Energy & Environmental Science

PAPER

View Article Online
View Journal | View Issue

Cite this: *Energy Environ. Sci.*, 2016, **9**, 1430

Enhancing the cycling stability of Na-ion batteries by bonding SnS_2 ultrafine nanocrystals on amino-functionalized graphene hybrid nanosheets†

Yong Jiang,[a] Min Wei,[a] Jinkui Feng,[a] Yuchen Ma[a] and Shenglin Xiong*[ab]

Received 24th October 2015,
Accepted 8th February 2016

DOI: 10.1039/c5ee03262h

www.rsc.org/ees

Room-temperature Na-ion batteries (NIBs) have been generally expected to offer a hopeful perspective for renewable energy storage applications on a large scale. However, a shortage of appropriate anode materials for NIBs has hindered their large-scale applications. Here, we report the strong chemical bonding of tin sulfide on amino-functionalized graphene that is prepared by a facile amine-thermal reaction. In contrast to previous reports on graphene-based composite electrodes, our strategy has the following merits: the one-step formation of amino-functionalized reduced grapheme oxide (RGO) from GO and tight contact of SnS_2 nanocrystals at an amino-functionalized graphene interface. This concept has been demonstrated by experimental results which are in congruence with first principles theoretical calculations. When investigated as an anode material for NIBs, the composite maintained a capacity of 680 mA h g^{-1} after cycling for 100 cycles at a current density of 200 mA g^{-1}, and 480 mA h g^{-1} after 1000 cycles at 1 A g^{-1}. The outstanding performance results from the unique structure of the hybrid nanosheets.

Broader context

NIBs have attracted more and more interest because sodium resources are abundant and inexpensive, which makes Na-ion systems more appropriate for large-scale energy storage than current Li-ion batteries (LIBs). However, the lack of anode materials with high capacity and long cycling stability has blocked the application of NIBs. In this work, ultrafine SnS_2 nanocrystals bonded on amino-functionalized graphene were easily synthesized at a low temperature of just 95 °C. Both experimental results and first principles theoretical calculations demonstrate the strong affinity of SnS_2 for the organic groups. Benefiting from their structural features, the prepared composites can deliver a reversible capacity of 480 mA h g^{-1} at 1 A g^{-1} after 1000 cycles with a capacity retention of 85% which is much higher than 43.8% for SnS_2 distributed on pristine graphene. Taking into consideration the outstanding performance and the facile synthesis process, this work could provide a promising strategy for developing nanocomposites with an excellent electrochemical ability.

Introduction

LIBs have permeated our daily lives over the past three decades. As a congener of lithium, sodium displays similar electrochemical behavior.[1] Given the abundant resources and low cost of sodium, Na-ion batteries (NIBs) have been generally considered to be more competitive than commercial LIBs for large-scale applications.[2,3] However, among the anode materials suitable for LIBs, most of them lose their excellent electrochemical properties when acting as electrodes for NIBs. Taking graphite for example, a lithiation and delithiation process can reversibly take place between the layers. A much lower capacity, less than 35 mA h g^{-1}, can be attained when graphite acts as an anode for NIBs.[4–6] Although, for metals (*e.g.*, Sn and Sb) and metal oxides (*e.g.*, SnO_2, Fe_2O_3 and CuO)[7–11] a much higher capacity can be obtained, cycling stability is disappointing due to large volume variations in the processes of charging and discharging. The fact that the ionic radius of Na^+ ions is larger than that of Li^+ ions is the crucial factor in all of the above electrochemical problems. As a result, extensive exploration of appropriate anode materials with high reversible capacity, long cycling stability and high Coulombic efficiency is of high necessity and urgency for NIBs.

Layered metal sulfides, such as WS_2, SnS_2, SnS and MoS_2, possess a large interlayer spacing. This open framework is beneficial for the mass transport of Na^+ ions, which are approximately 55% larger than Li^+ ions.[12–16] Nevertheless, the low conductivity inherent in these layered metal sulfides makes it difficult for them to have adequate electrochemical performances. At the same time, although the deleterious volume variations

[a] *Key Laboratory of Colloid and Interface Chemistry, Ministry of Education, and School of Chemistry and Chemical Engineering, Shandong University, Jinan 250100, China. E-mail: chexsl@sdu.edu.cn*

[b] *Institute of Physical Chemistry, Zhejiang Normal University, Jinhua 321004, China*

† Electronic supplementary information (ESI) available: FTIR, Raman, XPS, and more TEM (HRTEM, as well as electrochemical data). See DOI: 10.1039/c5ee03262h

accompanying Na-ion insertion–extraction processes can be compensated to some extent by the particular structure of layered metal sulfides,[15] the integrity of electrodes is finally damaged due to unavoidable volume changes. The above drawbacks hamstring the perspective that layered metal sulfides can behave well as anodes for NIBs. Up to now, carbonaceous materials have usually been integrated with metal sulfides to improve electrochemical performance.[17,18] In particular, reduced graphene oxide (RGO) with good conductivity, large surface area and outstanding flexibility can work as matrix for loading layered materials to effectively strengthen electrical conductivity, prevent aggregation and buffer mechanical variation. Various SnS_2/RGO nanostructures have been designed to improve electrochemical performance in LIBs.[19–24] Recently, nanocomposites composed of layered metal sulfides and graphene have been investigated in NIBs based on a similar strategy. For example, Su *et al.* prepared a WS_2@graphene nanocomposite that delivered a reversible capacity of 584 mA h g^{-1}.[12] Xie *et al.* demonstrated that the heterointerfacial area in the MoS_2/RGO heterostructure helped to improve the capacity of nanocomposites.[13] A hybrid structure containing SnS and graphene exhibited a stable capacity of 940 mA h g^{-1} at 30 mA g^{-1} after 50 cycles.[14] SnS_2–RGO composites also perform a high reversible capacity and prolonged cycling stability.[3,15,25,26] However, as a representative "2D" material, graphene itself cannot efficiently immobilize active material (and its discharge products) and thus cannot prevent them from aggregating inside a composite because of its planar geometry.[27,28]

It has been demonstrated that the remarkable chemical interactions between graphene and active materials as well as its discharge products can greatly improve the electrochemical performance of composites due to the synergism between chemically modified graphene and loaded foreign materials. For example, Zhou *et al.* reported that SnO_2 nanocrystals could be bound on nitrogen-doped RGO by Sn–N bonding, which is helpful for restricting the agglomeration of tin.[29] Gao *et al.* have made it clear that nitrogen doped graphene is able to boost the oxygen evolution performance of $CoSe_2$ nanobelts.[30] Herein, for the first time, we propose a facile approach for binding SnS_2 nanocrystals by C–N–Sn bonding on EDA-functionalized RGO sheets to achieve SnS_2 nanocrystal/EDA-functionalized RGO composites (denoted as SnS_2 NC/EDA–RGO). In contrast to previous reports on graphene-based composite electrodes *via* anomalous self-assembly or post-incorporation of active materials, our proposal has the following advantages: (i) a one-step procedure combines the *in situ* formation of SnS_2 NC and EDA-functionalized RGO, which eases the preparation process. Moreover, uniform SnS_2 nanocrystals are homogeneously confined onto EDA–RGO sheets. (ii) The tight confinement of SnS_2 NC (and its discharge products) at the EDA–RGO interface suppresses the agglomeration of SnS_2 nanocrystals and tin nanoparticles during sodium ion insertion/extraction processes. (iii) The integration of SnS_2 nanocrystals with RGO renders the establishment of a circuit network for electrons within the composite electrode and allows for the growth of a stable solid electrolyte interphase (SEI) layer over the electrode materials. (iv) The thin graphene and the ultrafine SnS_2 nanocrystals shorten the distance of sodium ion diffusion. Furthermore, the graphene sheets play a role of mitigating the large volume change of SnS_2 nanocrystals. Based on the unique electrode configuration, when examined as an anode material for NIBs, the as-prepared SnS_2 NC/EDA–RGO electrodes manifest high reversible capacity, remarkable rate capability, and excellent cycling stability.

Experimental section

Synthesis of SnS_2 NC/EDA–RGO hybrid nanosheets

The graphene oxide used in this paper was prepared using a modified Hummers' method.[31] 60 mg of graphene oxide, which was preserved in deionized (DI) water, was diluted to 50 mL and further ultrasonicated for 30 minutes. 0.7 g of $SnCl_4{\cdot}5H_2O$ ($\sim$2 mmol) was dissolved in the above dispersion and stirred for three hours. Then, 0.3 g ($\sim$4 mmol) of thioacetamide was added. After half an hour, 80 μL of ethylenediamine (EDA) was injected and stirred for a further one hour. The obtained stable mixture was hydrothermally treated at 95 °C for 6 h. The products were centrifuged to separate from the solvent and washed with deionized water three times. Finally, the as-obtained SnS_2 nanocrystal/EDA-functionalized RGO composites were freeze-dried for 72 h. For comparison, free-standing SnS_2 crystals were obtained as per a similar process with the preparation of SnS_2 NC/EDA–RGO, but without the addition of GO and EDA. The composites in which SnS_2 was distributed on reduced graphene oxide (denoted as SnS_2/RGO) were prepared based on the above procedures for SnS_2 NC/EDA–RGO without the addition of EDA and reduced with $NaBH_4$ at 120 °C for another four hours.

Computational method

All calculations in this work have been carried out using the Vienna ab initio simulation package (VASP).[32,33] The exchange–correlation function employed the standard generalized gradient approximation of Perdew–Burke–Ernzerhof. The graphene structure was constructed as a polyaromatic hydrocarbon molecule containing 24 carbon atoms and 12 hydrogen atoms. The binding energy (BE) is obtained by calculating the energy difference between the summation of SnS_2 molecule (E_1) and EDA–RGO system (E_2) and SnS_2 NC/EDA–RGO system (E_{total}) (*i.e.* $E = E_1 + E_2 - E_{total}$).

Instrumentation and material characterization

The as-obtained samples were examined using different measurement techniques. X-ray powder diffraction (XRD) patterns of the as-prepared samples were obtained using a Bruker D8 advanced X-ray diffractometer (Cu K_α radiation, λ = 1.5418 Å). Field emission scanning electron microscopy (FE-SEM) images were obtained using a JEOL JSM-6700F SEM operated at 5 kV. Transmission electron microscopy (TEM) images, high-resolution TEM (HRTEM) images, high-angle annular dark-field scanning TEM (HAADF-STEM) images, and elemental maps were obtained using a JEOL JEM-ARM 200F field-emission atomic-resolution analytical microscope operated at an accelerating voltage of 200 kV. Atomic force microscopy (AFM) images were obtained using a Vecco Multimode V atomic force microscope using a tapping mode. X-ray photoelectron spectroscopy (XPS) spectra were

obtained using an ESCALAB 250 spectrometer (Perkin-Elmer). Thermal gravimetric analysis (TGA) of the samples was performed in air on a SHI-MADZU, TGA-50 thermal analyzer. Fourier transform-infrared spectroscopy (FTIR) spectra were taken on a Bruker ALPHA-T FTIR spectrometer. Raman spectra were recorded with a 514.5 nm wavelength on a JY LABRAM-HR confocal laser micro-Raman spectrometer at room temperature.

Electrochemical measurement

To prepare the electrode, the prepared material, carbon black and carboxymethyl cellulose (Aladdin) in a mass ratio of 8 : 1 : 1 were mixed together with deionized water acting as a dispersion medium. After being ground into a homogeneous slurry, the mixture was uniformly distributed on commercial Cu foil (Shenzhen BiYuan Electronics) to prepare electrodes with a thickness of about 200 μm. The deionized water was thoroughly evaporated at 60 °C under vacuum. After that, electrode disks of 12 cm in diameter were obtained. The load of active material on each disk was 1 ± 0.15 mg cm^{-2}. CR2032 coin-type cells were assembled with home made sodium foil as the counter electrode. Sodium foils with diameters of about 14 mm were prepared from sodium bulk (Aladdin, 99.7%) in a glove box under the protection of high purity argon. Glass fiber (Whatman) acted as a separator. The electrolyte used was that 1 M $NaClO_4$ dissolved in a mixture of ethylene carbonate and diethylene carbonate. Fluoroethylene carbonate was added into the electrolyte at the weight percent of about 5% to act as an additive which was beneficial in forming a stable SEI film. All of the assembly processes were conducted in a glove box under the protection of ultrapure argon. The water content was below 1 ppm and the oxygen content was below 3 ppm. Galvanostatic cycling tests at different current densities were conducted on a battery test station (LAND CT-2001A, Wuhan, China) from 0.01 V to 3.0 V. Electrochemical impedance spectroscopy was performed on an electrochemical workstation (CH 760D, Shanghai, China).

Results and discussion

The hybrid SnS_2 NC/EDA–RGO was synthesized through a facile amine-thermal method with a low temperature and subsequent freeze-drying step. Briefly, $SnCl_4{\cdot}5H_2O$ was added into a GO suspension at room temperature under magnetic stirring. The Sn^{4+} can be tightly adsorbed onto the surface of GO by virtue of electrostatic interactions with functional groups such as carboxyl, hydroxyl, and epoxy groups which are negatively charged and abundant. Then, 4 mmol of thioacetamide was introduced into the above suspension and stirred for 30 min, and finally EDA was added into the mixture and maintained at 95 °C for 6 h. The as-obtained products were finally freeze-dried, which generated an EDA-functionalized hybrid material SnS_2 NC/EDA–RGO, with *ca.* 75 wt% SnS_2 in the composite based on TGA tested in an atmospheric environment (Fig. S1, ESI†). The hybrid material of SnS_2 nanocrystals and un-functionalized RGO (denoted as SnS_2/RGO) was also prepared through reduction with $NaBH_4$. Experimental details are described in the Experimental section.

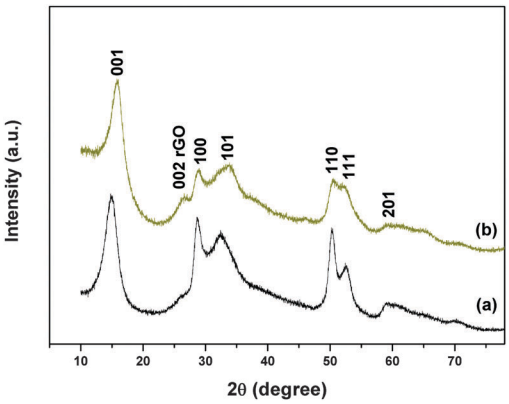

Fig. 1 XRD patterns of SnS_2 nanocrystals (a) and SnS_2 NC/EDA–RGO hybrid nanosheets (b).

To confirm the phase structure of the SnS_2 NC/EDA–RGO, XRD measurements were performed on the as-prepared SnS_2 crystals and SnS_2 NC/EDA–RGO nanosheets. As shown in Fig. 1, the diffraction pattern of SnS_2 (*i.e.* curve a) can be readily assigned to hexagonal SnS_2 (JCPDS card no. 23-0677). The XRD spectrum of SnS_2 NC/EDA–RGO hybrid nanosheets (curve b) displays a new broad peak at around 25.9° (about 0.34 nm), which originates from the (002) plane of few-layer reduced graphene. By comparison with those of pristine GO,[15] which features a characteristic diffraction peak at 11.2°, the XRD results demonstrate the reduction of GO during the moderate amine-thermal reaction. It should be noted that the broad diffraction features of SnS_2 reveal the small size of the SnS_2 nanoparticles.

FESEM, TEM, HRTEM, and HAADF-STEM were performed to investigate the microstructures of the SnS_2 NC/EDA–RGO hybrid nanosheets. As can be seen, the FESEM images (Fig. 2A and B) indicate that the as-prepared hybrid material displays a sheet-like structure with abundant and uniform nanocrystals dispersed on the surface. TEM images (Fig. 2C and Fig. S2, ESI†) further show that uniform and ultrafine nanocrystals are homogeneously distributed on the graphene sheets. HRTEM images (Fig. 2D and Fig. S3, ESI†) show that SnS_2 nanocrystals ranging from 2 to 4 nm in size were pinned onto the surfaces of graphene sheets with vacancies between particles, consistent with the broad XRD peaks observed. The ultrafine particles and developed vacancies are beneficial for accommodating volume variation and the infiltration of the electrolyte during cycling tests. The HRTEM images also reveal the few-layered (<3 layers) feature of EDA–RGO, as denoted by the arrows in Fig. 2D and Fig. S3 (ESI†). More credible information on the thickness of the SnS_2 NC/EDA–RGO hybrid nanosheets was achieved from the AFM image and the corresponding height profile is indicated in Fig. S4 (ESI†). Clearly, the average thickness of the hybrid nanosheets is estimated to be ~ 5 nm, in accordance with the HRTEM results. Fig. 2E shows a representative HAADF-STEM image of a few pieces of the SnS_2 NC/EDA–RGO hybrid nanosheets. The transparent feature of SnS_2 NC/EDA–RGO reveals that it is made up of extremely thin few-layered sheets. Fig. 2F shows the HAADF-HRTEM image recorded from the area marked by a white box in Fig. 2E. In the HAADF-HRTEM image, the lattice spacings

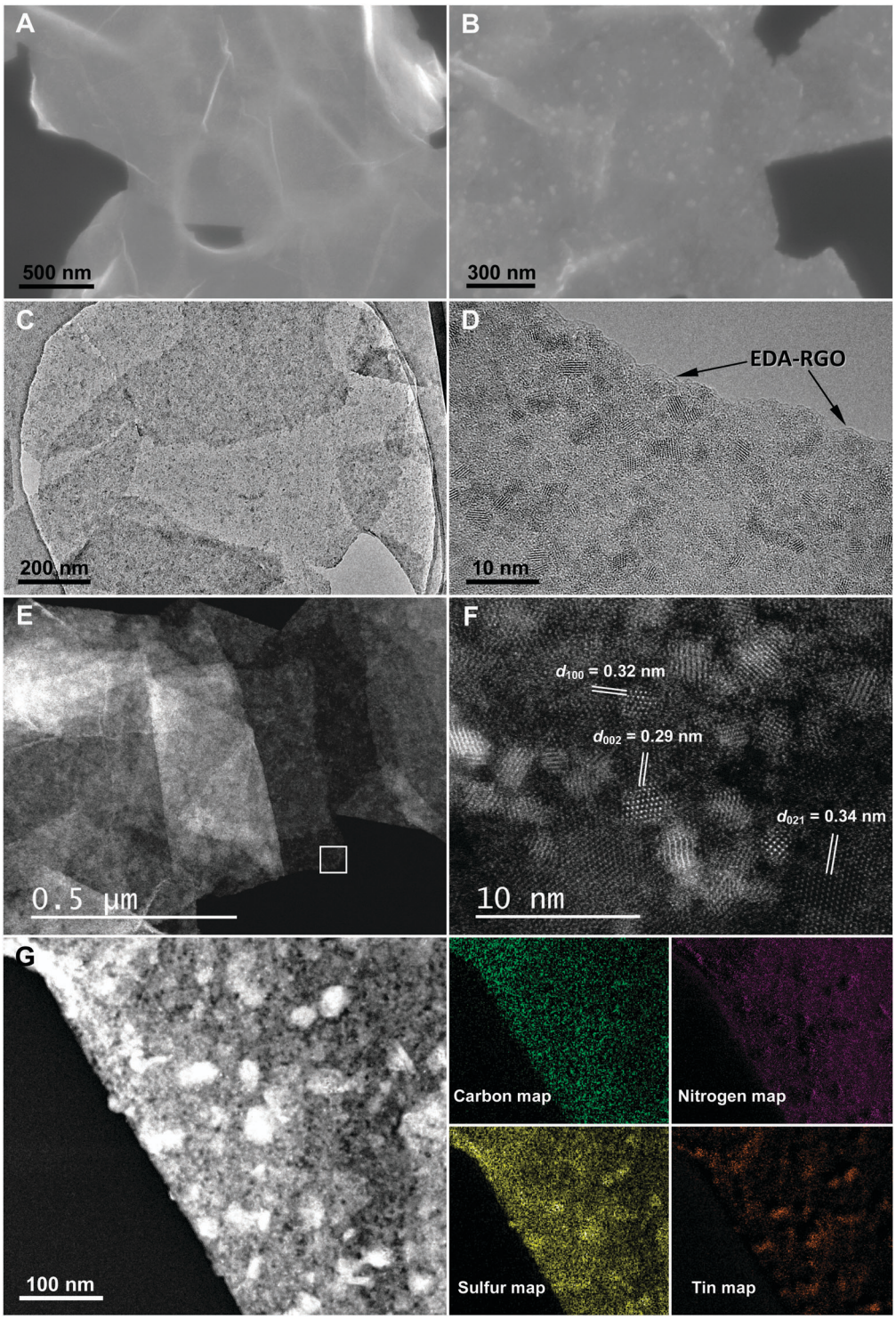

Fig. 2 Characterization of the SnS_2 NC/EDA–RGO hybrid nanosheets by electron microscopy. FESEM (A) and high-magnification FESEM (B) images of SnS_2 NC/EDA–RGO. TEM (C) and HRTEM (D) images of SnS_2 NC/EDA–RGO. (E) HAADF-STEM image of SnS_2 NC/EDA–RGO. (F) HAADF-HRTEM image marked by the white box in (E). (G) HAADF image and the corresponding C, N, S, and Sn elemental maps.

of 0.32 nm and 0.29 nm can be ascribed to $d_{(100)}$ and $d_{(002)}$ of hexagonal SnS_2, respectively. Very interestingly, we noted that the lattice spacing of 0.34 nm could be indexed to $d_{(021)}$ of orthorhombic SnS, suggesting the existence of trace orthorhombic SnS (JCPDS no. 83-1758) during the moderate amine-thermal reaction. The corresponding elemental maps of C, N, Sn, and S from the HAADF-STEM image (Fig. 2G) show a homogeneous spatial distribution through the whole scanning region, further verifying the uniform growth of SnS_2 nanocrystals and successful EDA functionalization of the graphene surface.

FTIR spectra were recorded to further characterize the constitution of SnS_2 NC/EDA–RGO. Bare EDA–RGO was also detected for comparison with the SnS_2 NC/EDA–RGO. As shown in Fig. S5A (ESI†), the bands at 3430 cm^{-1} and 1640 cm^{-1} are ascribed to the –OH groups of water molecules and RGO, respectively. In the case of EDA–RGO, the absorption peaks at 1398 cm^{-1} and 1436 cm^{-1} are assigned to C–N and $-CH_2$ groups respectively,[28,34,35] while the peak at 2913 cm^{-1} can be assigned to the N–H stretching mode similar to that observed in polyaniline.[35] The appearance of these peaks indicates that EDA can partially reduce GO and chemically functionalize RGO at the same time. For SnS_2 NC/EDA–RGO, most of the characteristic band locations were the same as EDA–RGO except that the peak of N–H was shifted to 3082 cm^{-1}. This spectral migration is probably due to the interaction between SnS_2 and the nitrogen atoms of EDA. The electropositive Sn^{4+} in SnS_2 probably had an inductive effect with the nitrogen element. Raman spectra (Fig. S5B, ESI†) for GO, EDA–RGO, and SnS_2 NC/EDA–RGO all display a D band at about 1324 cm^{-1} induced by sp^3 defects and a G band at about 1591 cm^{-1} typical of sp^2-bonded pairs.[30] The I_D/I_G ratio of the SnS_2 NC/EDA–RGO nanosheets indicates a remarkable increase compared with the values of GO and EDA–RGO, suggesting that variation of the graphite plane structure is triggered by the partial removal of oxygen-involved functional groups and additional defects introduced by surface EDA and SnS_2 nanocrystals.

To further explore the physicochemical nature of EDA–RGO and SnS_2 NC/EDA–RGO, the surface features of GO, EDA–RGO, and SnS_2 NC/EDA–RGO were investigated by XPS. The scanned C 1s spectrum of GO in Fig. 3A can be deconvoluted into four peaks of C–C (284.6 eV, sp^2-hydridized carbon), C═O (287.3 eV), C–O (286.6 eV), and O–C═O (288.8 eV).[28,34] Clearly, from GO to EDA–RGO and SnS_2 NC/EDA–RGO (Fig. 3A–C), the intensities of sp^2-hydridized carbon continually increase while those of functional groups corresponding to the oxygenous part considerably decline, revealing that the oxygen-involved groups were seriously extracted, *i.e.*, GO was reduced and graphene formed. Simultaneously, both the emergence of a C–N peak (285.6 eV)[28,30,34] and the observed change of sp^2-hybridized carbon along with oxygenous groups reveal partial restoration of the graphene structure and the effective functionalization of RGO during the moderate amine-thermal reaction (Fig. 3B and C), which is consistent with the FTIR results. The high-resolution N 1s spectrum of EDA–RGO in Fig. 3D can be fitted to three peaks of pyridinic N (398.8 eV), pyrrolic N (399.9 eV), and amino N (401.5 eV).[30] For SnS_2 NC/EDA–RGO, the N 1s spectrum shows a similar trend to that of EDA–RGO except for a positive shift in binding energies (BEs) (Fig. 3E and Fig. S6, ESI†), which shows similarity with the phenomenon observed in FTIR. All of these observations indicate charge-transfer from EDA–RGO to SnS_2 NC after combination.[30,36] The Sn 3d spectrum (Fig. 3F) shows two peaks with BE values at 487.0 and 495.4 eV, assigned to the Sn $3d_{5/2}$ and Sn $3d_{3/2}$ photoelectron emissions, respectively, consistent with a previous report for Sn^{4+}.[3] The interaction between Sn^{4+} and nitrogen element in SnS_2 NC/EDA–RGO causes an alteration in the chemical environment of nitrogen compared to that in

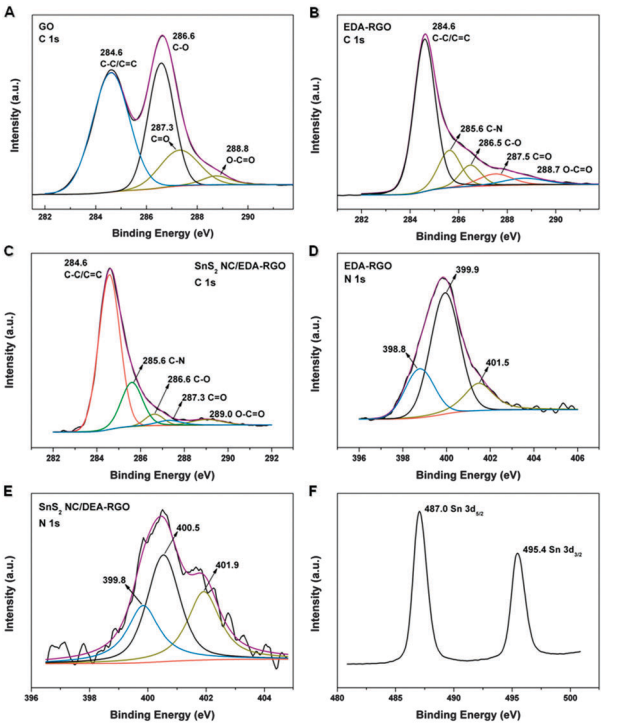

Fig. 3 XPS spectra analysis. High-resolution C 1s XPS spectra of (A) GO, (B) EDA–RGO, and (C) SnS_2 NC/EDA–RGO hybrid nanosheets. (D) High-resolution N 1s spectrum of EDA–RGO. (E) High-resolution N 1s spectrum of SnS_2 NC/EDA–RGO hybrid nanosheets. (F) High-resolution Sn 3d spectrum of SnS_2 NC/EDA–RGO hybrid nanosheets.

EDA–RGO, wherein the nitrogen element is more positively charged and thus the BE value is increased after the loading of SnS_2 NC.[30,36] All of the above results and discussion confirm that in our hybrid nanosheets, SnS_2 nanocrystals can bind with EDA–RGO *via* interfacial chemical bonding that fastens SnS_2 nanocrystals and hence, improves the electrical conductivity of the resultant hybrid material. Such a structure could effectively inhibit the exfoliation of active materials during repeated Na^+ insertion/extraction. In brief, the EDA–RGO in our unique SnS_2 NC/EDA–RGO hybrid architecture fulfils a dual role as a simultaneous electronic conductive channel and SnS_2 nanocrystal holder.

To confirm the microstructural benefits of SnS_2 NC/EDA–RGO and interfacial mediation for enhanced battery behaviour, systematic electrochemical tests were performed using CR2032 coin cells. SnS_2 NC/EDA–RGO composites were used as the electrode and home made sodium foil acted as a counter electrode. All the capacity values in this work are based on the mass of SnS_2. Fig. 4A shows the galvanostatic discharge–charge profiles for the 1st, 3rd, and 5th cycles of SnS_2 NC/EDA–RGO at a current density of 200 mA g^{-1}. The first discharge and charge capacities were 1025 mA h g^{-1} and 749 mA h g^{-1} respectively, corresponding to a Coulombic efficiency (CE) of 73%. The capacity loss and low CE in the first cycle largely pertain to the formation of an SEI as is referred to elsewhere.[3,12,15] We noted an obvious deviation in potential between charge and discharge cycles, which was significant and unfavourably affected energy efficiency. The voltage hysteresis present here originates from the combined

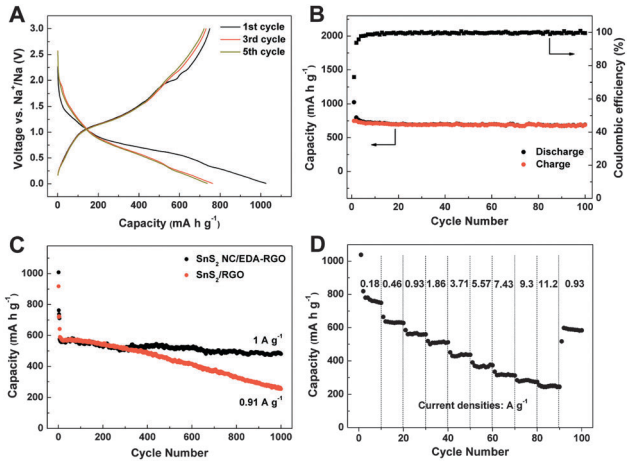

Fig. 4 Electrochemical performance of an SnS_2 NC/EDA–RGO electrode as a NIB anode. (A) Discharge–charge voltage profiles at a current density of 200 mA g^{-1}. (B) Cycling performance and CE at a current density of 200 mA g^{-1}. (C) Cycling performance of the SnS_2 NC/EDA–RGO anode at a current density of 1 A g^{-1}, in comparison with a SnS_2/RGO anode. (D) The discharge capacities at different current densities from 0.18 to 11.2 A g^{-1} of the SnS_2 NC/EDA–RGO anode.

results of the conversion reactions of SnS_2, alloying process of Sn and large ionic radius of Na^+. The solution will be further studied in near future. CE was quickly increased to about 99% in the following several cycles and kept at nearly 100% thereafter, as indicated in Fig. 4B. After 100 cycles at a rate of 200 mA g^{-1}, a reversible capacity as high as about 680 mA h g^{-1} was sustained (Fig. 4B). However, in the case of pure SnS_2, the first discharge and charge capacities were only 573 mA h g^{-1} and 144 mA h g^{-1}, respectively, at the current density of 200 mA g^{-1}. The discharge capacity seriously declined to 43 mA h g^{-1} after 100 cycles (Fig. S7, ESI†). The obvious difference between pure SnS_2 and SnS_2 NC/EDA–RGO indicates that with the aid of EDA-functionalized RGO, the electrochemical performance of the designed nanocomposites was remarkably promoted.

To explore the superiority of the unique SnS_2 NC/EDA–RGO nanosheets as anode materials for NIBs, we tested the long term cycling performance of the SnS_2 NC/EDA–RGO composite electrode at a current density of 1 A g^{-1} (Fig. 4C). The long-term cycling test was first activated at 200 mA g^{-1} for 5 cycles and then cycled at 1 A g^{-1} for 1000 cycles. The discharge capacities at the 10th and 1000th cycles at 1 A g^{-1} were 563 mA h g^{-1} and 480 mA h g^{-1}, respectively. The capacity at the 1000th cycle retained 85% of that at the 10th cycle. For the bare EDA-functionalized RGO electrode (Fig. S8, ESI†), the observed capacity was less than 30 mA h g^{-1}, illustrating that the capacity contribution from EDA–RGO could be ignored for SnS_2 NC/EDA–RGO. For comparison, SnS_2/RGO was also investigated under the same conditions (Fig. 4C). The discharge capacities at the 10th cycle and 1000th cycle were 583.5 mA h g^{-1} and 255.6 mA h g^{-1}, respectively, corresponding to a capacity retention of only 43.8%, which is much lower than the 85% of SnS_2 NC/EDA–RGO. These results illustrate that EDA-functionalized RGO has a superior ability to sustain capacity stability in comparison with pristine RGO.

As expected, the SnS_2 NC/EDA–RGO composite electrode presents superior high rate capability. As indicated in Fig. 4D, the SnS_2 NC/EDA–RGO delivered capacities of 760 mA h g^{-1}, 630 mA h g^{-1}, 560 mA h g^{-1}, 510 mA h g^{-1},435 mA h g^{-1}, 370 mA h g^{-1}, 315 mA h g^{-1}, 280 mA h g^{-1}, and 250 mA h g^{-1} at current densities of 0.18 A g^{-1}, 0.46 A g^{-1}, 0.93 A g^{-1}, 1.86 A g^{-1}, 3.71 A g^{-1}, 5.57 A g^{-1}, 7.43 A g^{-1}, 9.3 A g^{-1}, and 11.2 A g^{-1}, respectively. When the current density was abruptly switched back to 0.93 A g^{-1}, the discharge capacity was recovered to 580 mA h g^{-1} which was equal to the original value, suggesting that the highly robust structure of SnS_2 NC/EDA–RGO was not damaged even when cycled at a jumpy current density. Layered metal sulfides have been generally considered to be appropriate candidates for NIB anode materials, especially when combined with another carbon matrix. As shown in Table S1 (ESI†), the sodium storage properties obtained in the current study were compared with many other layered metal sulfides, including SnS_2/RGO,[3,15] GO–SnS_2-300,[25] SnS@graphene,[14] WS_2@graphene composites[12] and MoS_2/carbon composites.[13,17,18] Obviously, SnS_2 NC/EDA–RGO hybrid nanosheets in the present study performed the best when considering the reversible capacity and cycling stability.

To shed more light onto the electrochemical process of SnS_2 NC/EDA–RGO, the electrode materials after 700 cycles at a current density of 1 A g^{-1} were collected for further analysis using TEM, selected-area electron diffraction (SAED) patterns, HRTEM, and corresponding element mapping. The SAED pattern of SnS_2 NC/EDA–RGO after 700 cycles reveals a polycrystalline nature, which can be assigned to hexagonal SnS_2, as also demonstrated by the HRTEM image (Fig. 5A and B). Very importantly, we noted that the spacing between adjacent fringes was *ca.* 0.34 nm, close to the theoretical interplane spacing of orthorhombic SnS (021) planes which is consistent with the above HADDF-HTREM results. Combined with the TEM and HRTEM images, the carbon, nitrogen, sulfur, and tin element mappings indicate that the homogeneous distribution of nanocrystals in EDA–RGO sheets is maintained as well as before cycling (Fig. 5C and D), which reveal that the strong chemical affinity of SnS_2 for EDA–RGO is helpful to suppress aggregation of the generated tin nanoparticles during sodium insertion. The above discussion illustrates that the structural sturdiness of SnS_2 NC/EDA–RGO was kept well, even after long term cycling. In order to clearly understand the electrochemical mechanism of SnS_2 NC/EDA–RGO, *ex situ* XRD (Fig. S9A, ESI†), together with *ex situ* HRTEM (Fig. S9B–D, ESI†), was conducted to monitor samples collected at different discharge/charge voltages to follow the changes of state of tin. As shown in Fig. S9A (ESI†), when sodiation proceeded to 0.56 V, SnS, Sn and Na_2S can be detected, which was also confirmed by the corresponding HRTEM image (Fig. S9B, ESI†). After completely discharging to 0.01 V, the peaks of Na_2S and Sn were still resolved, while the signals corresponding to SnS disappeared (Fig. S9A and C, ESI†). These results illustrated that the transformation of SnS_2 to SnS occurred during the discharge process, accompanied with the conversion of SnS to Sn at the same time. After 0.56 V, the residual SnS gradually transformed to Sn and Na_2S. Na_xSn was not observed from *ex situ* XRD which

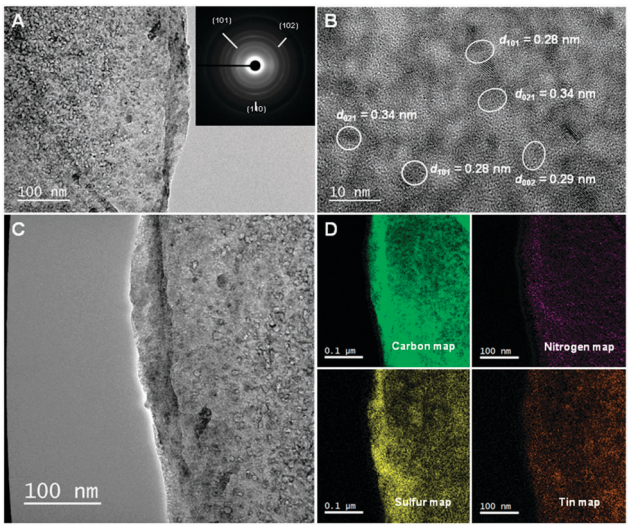

Fig. 5 TEM image (A), HRTEM image (B), and TEM image (C) and the corresponding C, N, S, and Sn elemental maps (D) of the SnS_2 NC@N–RGO electrode after 700 charge/discharge cycles. The inset in (A) is the corresponding SAED pattern.

was attributed to the poor crystallinity.[14,37] Upon charging to 3 V, the *ex situ* HRTEM (Fig. S9D, ESI†) shows the existence of SnS_2 and SnS. In addition, the *ex situ* XRD peaks of Na_2S can also be detected (Fig. S9A, ESI†). The coexistence of SnS_2, SnS and Na_2S indicate that the sodium storage reaction of SnS_2 NC/EDA–RGO should be partly reversible.[37] The as-synthesized SnS_2 NC/EDA–RGO, together with pure SnS_2 and SnS_2/RGO, were further tested by electrochemical impedance spectroscopy (EIS) measurements. All the electrodes were cycled three times and kept at the same cut-off voltage for EIS testing. The Nyquist plots (Fig. S10, ESI†) show that the semicircle diameter for the SnS_2 NC/EDA–RGO electrode in the high-medium frequency region is the smallest among the three prepared materials, revealing the lowest contact and charge-transfer resistance of SnS_2 NC/EDA–RGO, benefiting from the strong binding of SnS_2 and its discharge product with EDA–RGO. It is also evident that the electrical conductivity of SnS_2 NC/EDA–RGO is the highest and the charge-transfer reaction for sodium ions is the fastest.

All the above representations unambiguously confirm the formation of interfacial bonding in the SnS_2 NC/EDA–RGO hybrid nanosheets from our amine-thermal reaction. Herein, first principles theoretical calculations were conducted to further explore the mechanism by which surface functionalization of GO with EDA can strengthen interactions between SnS_2 nanocrystals and the conductive matrix (*i.e.* EDA-functionalized RGO). The calculation details are described in the Experimental section. The model system in our calculations is based on SnS_2 and single-layer graphene. In the case of SnS_2 NC/EDA–RGO, two kinds of nitrogen atoms, the pyrrolic nitrogen and the nitrogen atom of $–NH_2$ in EDA–RGO were targeted. For comparison, pristine RGO without functional groups was also modelled under the same conditions. The optimized results of SnS_2 interaction with EDA–RGO are shown in Fig. 6. The binding energies (BE) of SnS_2 clusters with different graphene matrixes were calculated to discriminate the adhesion level. The BE of SnS_2/pristine RGO is only 0.018 eV (Fig. 6A). After EDA functionalization, the binding energy can reach as high as 0.851 eV through the interaction of SnS_2 with the nitrogen atom in $–NH_2$ extruding out (Fig. 6C). Moreover, SnS_2 can also bind with both nitrogen atoms with a higher binding energy, *i.e.* 1.230 eV (Fig. 6D). The binding energy between pyrrolic nitrogen and SnS_2 is also calculated to be 0.620 eV. This striking distinction indicates the strong adhesion of SnS_2 to the amino-functionalized carbon matrix. Specifically, EDA moieties can adhere to RGO through strong chemical bonding, which can also be verified by first principles calculations. The BE between EDA and RGO is 1.268 eV (Fig. 6B). It should be noted that one of the discharge products, sodium sulfide, for the SnS_2 NC/EDA–RGO electrode can be fixed by amino-containing functional groups, which is also testified by calculations. Fig. S11 (ESI†) shows the optimized models. The BE between pristine RGO and Na_2S is only 0.250 eV (Fig. S11A and B, ESI†). For EDA–RGO, Na_2S can bind to one or two nitrogen atoms with BEs of 0.728 eV and 1.303 eV (Fig. S11C and D, ESI†), respectively. First principles calculations give us confirmation that the chemically modified graphene has the stronger affinity for SnS_2, as well as the discharge product Na_2S, probably *via* the formation of C–N–Sn and C–N–Na bonds, which imparts a significant improvement on cycling and rate performance.

As discussed above, the strong interactions between SnS_2 and EDA–RGO have been clarified by experimental results and theoretical calculations. Moreover, EDA, an ideal crosslinker, also has an interrelation with the discharge products. Graphene is a good encapsulating material for active nanomaterials with the advantages of a large surface area, high mechanical flexibility, and excellent conductivity. When small SnS_2 nanoparticles are pinned on EDA–RGO, the complicated substrate networks can facilitate the transmission of electron and sodium ions in a 2D pathway. The strong chemical bonding on the SnS_2 NC/EDA–RGO interface and

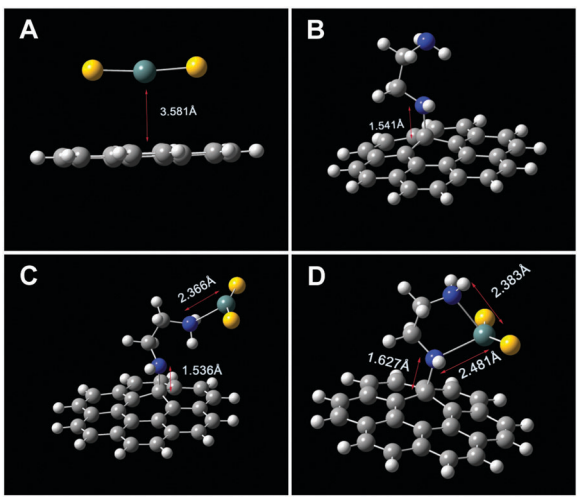

Fig. 6 The models of VASP calculation, showing the interactions between SnS_2 and pristine graphene (A), and EDA modified graphene (C and D). Figure (B) shows the EDA absorbed on graphene. The carbon (C), sulphur (S), tin (Sn), hydrogen (H) and nitrogen (N) atoms are denoted by gray, yellow, celadon, white and blue spheres respectively.

its discharge products effectively inhibits the destruction of the electrode structure and the aggregation of discharge products during repeated Na^+ insertion/extraction. The small size of SnS_2 nanocrystals is favorable for rapid reactions with Na ions due to a shortened Na-ion diffusion path. At the same time, there is ample space between nanocrystals which is beneficial for the electrolyte to permeate the active framework. The free space and small size, together with the good flexibility of EDA–RGO, are able to effectively buffer the mechanical stress generated during cycling. The fact that SnS_2 NC/EDA–RGO delivers a better cycling stability than RGO/SnS_2 reveals that the strong chemical bonding of SnS_2 nanocrystals and the discharge products on graphene sheets functionalized with EDA is an indispensable factor for the exceptionally long lifespan of the SnS_2 NC/EDA–RGO electrode.

Conclusions

In conclusion, we have experimentally achieved and theoretically estimated a moderate amine-thermal reaction that is facile and effective for the large-scale fabrication of SnS_2 NC/EDA–RGO hybrid materials. Ultrafine SnS_2 nanocrystals were uniformly immobilized on a EDA–RGO surface by virtue of a synchronous reduction and functionalization process. Upon use as anode material in NIBs, the combination of ultrafine SnS_2 nanocrystals and highly conductive graphene synergistically enhances the ion and charge transfer kinetics of the SnS_2 NC/EDA–RGO nanocomposite. What's more, the vigorous chemical interaction on the SnS_2 NC/EDA–RGO interface derived from the EDA bridging role between nanocrystals and nanosheets, as well as the discharge products, can effectively strengthen physicochemical interactions, and hence essentially improves the reversible capacity, rate profile and cycling performance of the SnS_2 NC/EDA–RGO nanocomposite. The exceptional performance with an inexpensive and versatile synthesis strategy suggests that the as-developed methodology may provide a viable vision for the application of NIBs.

Acknowledgements

The authors thank the National Natural Science Fund of China (Grant No. 21371108, 21203110, 21433006, and 21573131), Shandong Provincial Natural Science Foundation for Distinguished Young Scholars (JQ201304), and Key Laboratory of the Ministry of Education for Advanced Catalysis Materials, Zhejiang Normal University, Jinhua 321004, China (ZJHX201505) for financial support.

Notes and references

1 C. Luo, Y. Zhu, Y. Xu, Y. Liu, T. Gao, J. Wang and C. Wang, *J. Power Sources*, 2014, **250**, 372–378.
2 P. Barpanda, G. Liu, C. D. Ling, M. Tamaru, M. Avdeev, S.-C. Chung, Y. Yamada and A. Yamada, *Chem. Mater.*, 2013, **25**, 3480–3487.
3 Y. Zhang, P. Zhu, L. Huang, J. Xie, S. Zhang, G. Cao and X. Zhao, *Adv. Funct. Mater.*, 2015, **25**, 481–489.
4 Y. Wen, K. He, Y. Zhu, F. Han, Y. Xu, I. Matsuda, Y. Ishii, J. Cumings and C. Wang, *Nat. Commun.*, 2014, **5**, 4033.
5 P. Ge and M. Fouletier, *Solid State Ionics*, 1988, **28–30**, 1172–1175.
6 D. A. Stevens and J. R. Dahn, *J. Electrochem. Soc.*, 2001, **148**, A803–A811.
7 L. Liang, Y. Xu, C. Wang, L. Wen, Y. Fang, Y. Mi, M. Zhou, H. Zhao and Y. Lei, *Energy Environ. Sci.*, 2015, **8**, 2954–2962.
8 Y. Liu, Y. Xu, Y. Zhu, J. N. Culver, C. A. Lundgren, K. Xu and C. Wang, *ACS Nano*, 2013, **7**, 3627–3634.
9 Y.-X. Wang, Y.-G. Lim, M.-S. Park, S.-L. Chou, J. H. Kim, H.-K. Liu, S.-X. Dou and Y.-J. Kim, *J. Mater. Chem. A*, 2014, **2**, 529–534.
10 Z. Jian, B. Zhao, P. Liu, F. Li, M. Zheng, M. Chen, Y. Shi and H. Zhou, *Chem. Commun.*, 2014, **50**, 1215–1217.
11 L. Wang, K. Zhang, Z. Hu, W. Duan, F. Cheng and J. Chen, *Nano Res.*, 2014, **7**, 199–208.
12 D. Su, S. Dou and G. Wang, *Chem. Commun.*, 2014, **50**, 4192–4195.
13 X. Xie, Z. Ao, D. Su, J. Zhang and G. Wang, *Adv. Funct. Mater.*, 2015, **25**, 1393–1403.
14 T. Zhou, W. K. Pang, C. Zhang, J. Yang, Z. Chen, H. K. Liu and Z. Guo, *ACS Nano*, 2014, **8**, 8323–8333.
15 B. Qu, C. Ma, G. Ji, C. Xu, J. Xu, Y. S. Meng, T. Wang and J. Y. Lee, *Adv. Mater.*, 2014, **26**, 3854–3859.
16 Y. Cao, L. Xiao, M. L. Sushko, W. Wang, B. Schwenzer, J. Xiao, Z. Nie, L. V. Saraf, Z. Yang and J. Liu, *Nano Lett.*, 2012, **12**, 3783–3787.
17 C. Zhu, X. Mu, P. A. Aken, Y. Yu and J. Maier, *Angew. Chem., Int. Ed.*, 2014, **53**, 2152–2156.
18 J. Wang, C. Luo, T. Gao, A. Langrock, A. C. Mignerey and C. Wang, *Small*, 2015, **11**, 473–481.
19 Z. Jiang, C. Wang, G. Du, Y. J. Zhong and J. Z. Jiang, *J. Mater. Chem.*, 2012, **22**, 9494–9496.
20 L. Mei, C. Xu, T. Yang, J. Ma, L. Chen, Q. Li and T. Wang, *J. Mater. Chem. A*, 2013, **1**, 8658–8664.
21 X. Jiang, X. Yang, Y. Zhu, J. Shen, K. Fan and C. Li, *J. Power Sources*, 2013, **237**, 178–186.
22 Q. Zhang, R. Li, M. Zhang, B. Zhang and X. Gou, *Electrochim. Acta*, 2014, **115**, 425–433.
23 L. Zhuo, Y. Wu, L. Wang, Y. Yu, X. Zhang and F. Zhao, *RSC Adv.*, 2012, **2**, 5084–5087.
24 S. Liu, X. Lu, J. Xie, G. Cao, T. Zhu and X. Zhao, *ACS Appl. Mater. Interfaces*, 2013, **5**, 1588–1595.
25 P. V. Prikhodchenko, D. Y. W. Yu, S. K. Batabyal, V. Uvarov, J. Gun, S. Sladkevich, A. A. Mikhaylov, A. G. Medvedev and O. Lev, *J. Mater. Chem. A*, 2014, **2**, 8431–8437.
26 Y. Liu, H. Kang, L. Jiao, C. Chen, K. Cao, Y. Wang and H. Yuan, *Nanoscale*, 2015, **7**, 1325–1332.
27 X. Yang, L. Zhang, F. Zhang, Y. Huang and Y. Chen, *ACS Nano*, 2014, **8**, 5208–5215.
28 Z. Wang, Y. Dong, H. Li, Z. Zhao, H. B. Wu, C. Hao, S. Liu, J. Qiu and X. W. Lou, *Nat. Commun.*, 2014, **5**, 5002.
29 X. Zhou, L.-J. Wan and Y.-G. Guo, *Adv. Mater.*, 2013, **25**, 2152–2157.
30 M.-R. Gao, X. Cao, Q. Gao, Y.-F. Xu, Y.-R. Zheng, J. Jiang and S.-H. Yu, *ACS Nano*, 2014, **8**, 3970–3978.

31 W. S. Hummers and R. E. Offeman, *J. Am. Chem. Soc.*, 1958, **80**, 1339.
32 G. Kresse and J. Furthmüller, *Comput. Mater. Sci.*, 1996, **6**, 15–50.
33 G. Kresse and J. Furthmüller, *Phys. Rev. B: Condens. Matter Mater. Phys.*, 1996, **54**, 11169–11186.
34 H. Hu, Z. Zhao, W. Wan, Y. Gogotsi and J. Qiu, *Adv. Mater.*, 2013, **25**, 2219–2223.
35 G.-C. Li, G.-R. Li, S.-H. Ye and X.-P. Gao, *Adv. Energy Mater.*, 2012, **2**, 1238–1245.
36 K. X. Yao and H. C. Zeng, *J. Phys. Chem. C*, 2007, **111**, 13301–13308.
37 W. Sun, X. Rui, D. Yang, Z. Sun, B. Li, W. Zhang, Y. Zong, S. Madhavi, S. Dou and Q. Yan, *ACS Nano*, 2015, **9**, 11371–11381.

